Nuclear-driven electron spin rotations in a single donor coupled to a silicon quantum dot

Patrick Harvey-Collard,[1,2,*] N. Tobias Jacobson,[3] Martin Rudolph,[2] Jason Dominguez,[2] Gregory A. Ten Eyck,[2] Joel R. Wendt,[2] Tammy Pluym,[2] John King Gamble,[3] Michael P. Lilly,[4] Michel Pioro-Ladrière,[1,5] and Malcolm S. Carroll[1,2,†]

[1]*Département de physique, Université de Sherbrooke, Sherbrooke, QC, J1K 2R1, Canada*
[2]*Sandia National Laboratories, Albuquerque, NM, 87185, United States*
[3]*Center for Computing Research, Sandia National Laboratories, Albuquerque, NM, 87185, United States*
[4]*Center for Integrated Nanotechnologies, Sandia National Laboratories, Albuquerque, NM, 87185, United States*
[5]*Quantum Information Science Program, Canadian Institute for Advanced Research, Toronto, ON, M5G 1Z8, Canada*
(Dated: December 1st, 2015)

Silicon chips hosting a single donor can be used to store and manipulate one bit of quantum information. However, a central challenge for realizing quantum logic operations is to couple donors to one another in a controllable way. To achieve this, several proposals rely on using nearby quantum dots (QDs) to mediate an interaction. In this work, we demonstrate the coherent coupling of electron spins between a single ^{31}P donor and an enriched ^{28}Si metal-oxide-semiconductor few-electron QD. We show that the electron-nuclear spin interaction on the donor can drive coherent rotations between singlet and triplet electron spin states of the QD-donor system. Moreover, we are able to tune electrically the exchange interaction between the QD and donor electrons. The combination of single-nucleus-driven rotations and voltage-tunable exchange provides every key element for future all-electrical control of spin qubits, while requiring only a single QD and no additional magnetic field gradients.

Silicon is the central material of modern microchip technology and happens to be an ideal host for the most natural of quantum bits: a quantum of spin [1]. In particular, donor spins in silicon exhibit extraordinarily long quantum coherence lifetimes [2, 3]. The recent demonstrations of high-fidelity coherent control of both electron and nuclear spins of a single donor in a silicon nanostructure [4] have boosted momentum to the quantum computer architecture first envisioned by Kane [5]. However, the next step of coupling donor atoms to one another in a controllable way has proven extremely challenging, requiring near-atomic precision in the placement of the donors [6–8]. Such fabrication requirements contribute to concerns about the viability of donor spins for quantum computing.

Here, we advance donor-based quantum information processing beyond the isolated single donor qubit by coherently coupling a phosphorus donor's electron spin to a metal-oxide-semiconductor (MOS) quantum dot (QD) in isotopically-enriched silicon. Quantum dots have been theoretically discussed as intermediates to couple donor qubits in many different work [5, 9–13]. In our system, the QD is tuned to few-electron occupancy while simultaneously keeping a nearby donor (D) tunnel-coupled to the QD. This effectively forms a double-QD system where one of the QDs is replaced by the phosphorus atom. The donor-QD spin states are manipulated using a two-level singlet-triplet (ST) encoding analogous to those in double-QD qubits [14, 15]. Specifically, the two logical states are the singlet S and $m = 0$ triplet T_0. Our encoding takes advantage of the contact hyperfine interaction, $A\boldsymbol{S} \cdot \boldsymbol{I}$, between the donor electron spin $\boldsymbol{S}$ and donor nuclear spin $\boldsymbol{I}$, where A is the hyperfine coupling strength. This interaction makes the electron spin on the donor precess at a

rate $A/2$ different from the QD electrons. The hyperfine interaction thus amounts to an effective magnetic field gradient produced by the single phosphorus nucleus and drives rotations between singlet and triplet states [16]. By electrically controlling the donor charge configuration between ionized and neutral, the rotations can be turned off and on. The electron-electron exchange coupling and the hyperfine interaction with the donor nucleus define two orthogonal control axes for the qubit, and their relative strength is controlled using fast electrical pulses. Our donor-QD interaction relaxes the stringent constraints of direct donor-donor coupling in the bulk, since quantum dots are intrinsically larger and much more tunable than donors. Moreover, our approach lays the foundation for an efficient implementation of an all-electrical singlet-triplet spin qubit that eliminates the need for external micromagnets [17, 18] or additional QDs as in all-exchange qubits [19], and avoids the decoherence mechanisms associated with GaAs or Si host nuclear species [15, 20]. From a fundamental physics perspective, our approach provides a platform for studying the entanglement between electrons located at the MOS interface and in the bulk. We also gain access to a nuclear spin that could be harnessed as an additional resource in future experiments [9].

The QD-D device is fabricated with isotopically-enriched ^{28}Si and a foundry-compatible process (i.e. no lift-off processing). We use a poly-silicon gate stack, shown in Fig. 1A, that allows self-aligned ion implantation and subsequent activation annealing process. Phosphorus donors are implanted inside the red dashed rectangles using the AG gate as a mask. This processing maximizes the probability of placing a D in a suitable location next to the QD. It also facilitates future multi-qubit fabrica-
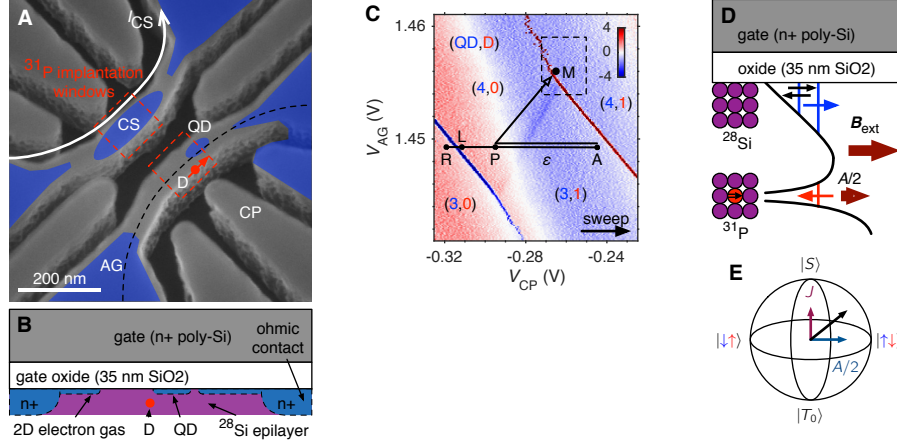
Figure 1. Quantum dot-donor device. (**A**) Angled-view scanning electron microscope image of the poly-Si gates above a 35 nm oxide. The blue overlay represents the 2D electron gas at the Si–oxide interface. Donors are implanted in the regions designated by the dashed red lines. The relevant donor location is indicated by the red dot. (**B**) Device gate stack along the dashed black line of Fig. 1A. (**C**) QD-D charge stability diagram. Overlaid are the different points of the experiment's pulse sequences. The detuning ϵ is defined along the black line with zero detuning at the center of the $(4, 0) \leftrightarrow (3, 1)$ transition. Color scale: $\mathrm{d}I_{\mathrm{CS}}/\mathrm{d}V_{\mathrm{CP}}$ (arb. u.). (**D**) Schematic vertical cut showing the QD electrons confined at the Si–oxide interface and separated by a valley splitting, together with the D potential. (**E**) Bloch sphere showing the logical ST qubit states at the poles. Electrical voltages adjust the relative magnitudes of J and $A/2$: J is dominant in the $(4, 0)$ configuration, while $A/2$ is in the $(3, 1)$ configuration.

tion that could take advantage of single ion implantation [6] and a planar QD geometry [12, 13]. Fabrication details are found in the Supplementary Material and are similar to Ref. [21]. A channel of electrons is formed at the MOS interface (Fig. 1B) underneath the wire-shaped accumulation gate (AG) by applying a positive voltage, depicted as a blue overlay in Fig. 1A. Next, a QD island is isolated by applying suitable negative voltages on neighboring gates. A single-electron transistor (SET) is formed in the upper wire to monitor the electron occupation N of the QD and the relevant donor, denoted $(N_{\mathrm{QD}}, N_{\mathrm{D}})$. The SET charge sensor (CS) is also used for spin readout via spin-to-charge conversion. Detailed information about fabrication, gate biasing and electron counting is provided in the Supplementary Material.

To investigate singlet-triplet dynamics, we first identify an effective $(2, 0) \leftrightarrow (1, 1)$ QD-D charge transition with a total of four electrons, as shown in Fig. 1C. Singlet-triplet states with more than two electrons have been studied theoretically [22] and experimentally [23] in double-QD systems. Using magnetospectroscopy [24–26], we verify that the QD spin filling is indeed consistent with having a four-electron singlet ground state (see Supplementary Material Fig. S1F). A requirement for efficient spin initialization and readout is that the energy difference J_{20} between the singlet $(2, 0)S$ and triplet $(2, 0)T_0$ be much larger than the electron temperature of the experiment [27], which is 215 mK in this case. In silicon, the valley splitting is generally the factor limiting J_{20} [28]. In our device and for the values of V_{AG} used, we have measured the valley splitting to be approximately 60 µeV. Consis-

tent with this observation, the two-electron QD states had similarly small values for J_{20}. The four-electron QD state of Fig. 1C, however, has an appreciably larger ST splitting of $J_{40} = 143$ µeV (as measured from both magnetospectroscopy and excited state spectroscopy). This might be understood as a shell filling effect with asymmetric QD orbitals, where the pairing of spins allows to circumvent the small valley splitting, as illustrated in the schematic of Fig. 1D [29].

Next, we show that we can initialize and read out ST spin states. To do so, we use the pulse sequence of Fig. 2A. The system is initialized into a $(4, 0)S$ or $(4, 0)T$ state by first ejecting the fourth electron at point R (as defined in Fig. 1C), and then loading either a S or T state by carefully tuning the load level of point L. A deeper load tends to prepare T states due to their ~ 10 times faster loading rate. After passing through an intermediate point P, which will be important for spin manipulations, the gate voltages are pulsed to point M for spin readout.

The readout mechanism is shown in Fig. 2B. Through Pauli-blockade, the spin state is converted to either a $(4, 0)$ or $(4, 1)$ charge state depending on whether the initial spin state was a singlet or a triplet, respectively. The mechanism relies on a charge hysteresis effect caused by the absence of direct access to a charge reservoir for the donor (Fig. 2C). Hence, the donor↔lead transitions are very slow because they have to go through a co-tunneling process to equilibrate [30]. Placing point M between the S and T charge preserving transitions then allows a fast relaxation path to the charge ground state only if the initial state was $(4, 0)T$. If the state was $(4, 0)S$, the sys-
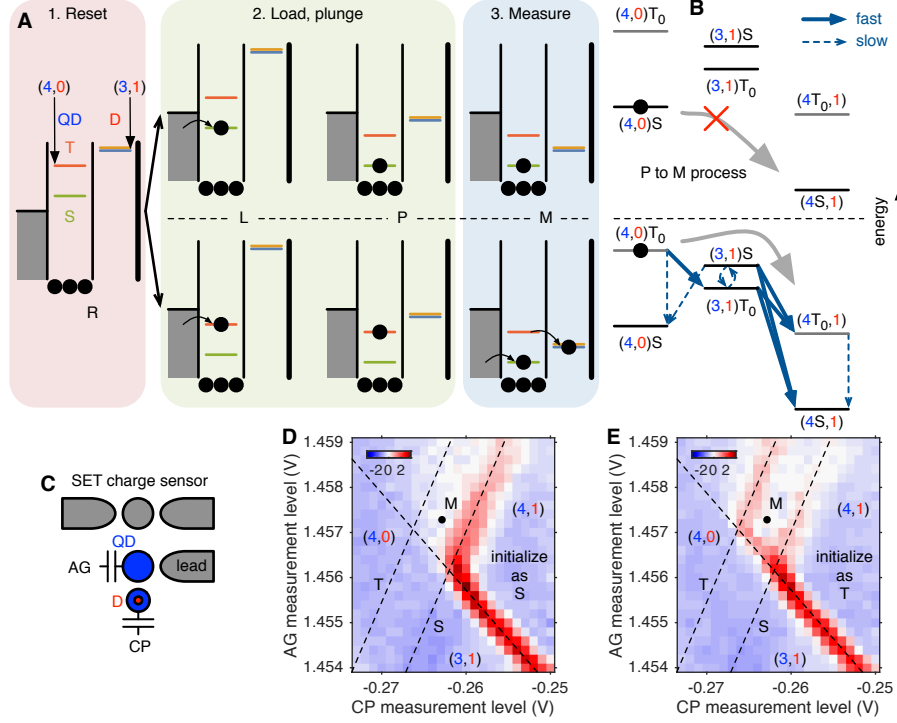
Figure 2. Spin preparation and readout. (**A**) Measurement pulse sequence. The state is reset by emptying the QD at point R (see Fig. 1C). A $(4,0)S$ or $(4,0)T$ is loaded at point L. After passing through point P, the system is biased to point M for readout. (**B**) Readout process at point M. If the state was $(4,0)S$, the system is locked in a metastable charge state. If the state was $(4,0)T$, the pulse is beyond the $(4,0) \leftrightarrow (3,1)$ transition line, which unlocks the relaxation to $(4,1)$ by going through $(3,1)$. (**C**) Schematic showing the QD-D configuration. The D has no direct connection to a lead, which causes the hysteresis. (**D-E**) Readout demonstration. The coordinates of point M (only) are swept across the charge stability diagram. When preparing predominantly S states, as in (D), only the S QD-D charge transition is visible. In contrast, preparing predominantly T states reveals the T QD-D charge transition, as in (E). The CS current at the location labeled M is then proportional to the triplet probability. Color scale: dI_{CS}/dV_{CP} (arb. u.).

tem is locked in a metastable charge configuration. The resulting CS signal is enhanced because the final charge configuration differs by one electron and lasts longer than the relaxation time of the $(4,0)T$ state. A charge enhancement effect like this has been previously highlighted by Studenikin *et al.* [31]. This readout mechanism allows us to use averaged measurements instead of single-shot. Since the measurement step is the longest in the pulse sequence, the current at point M in Fig. 2D-E is proportional to the triplet probability. All state measurements throughout this work are averaged over many (150 to 200) cycles. Details about the pulse sequence, loading rates, relaxation rates and probability calibration are given in the Supplementary Material.

Rotations between S and T_0 can be driven by an effective magnetic field gradient $\Delta B_z = A/2$ between the QD and the donor, as shown in Fig. 1E. These rotations provide a signature of the single ^{31}P donor. To demonstrate this effect, we use the pulse sequence shown in Fig. 3A. We prepare a $(4,0)S$ state by first emptying the QD and loading an electron between the singlet (S) and triplet (T) loading lines. We define zero detuning (the energy

difference ϵ between the QD and D) at the QD-D charge transition, and positive detunings along V_{CP} in the $(3,1)$ direction with a 17 µeV/mV lever arm. Then, we plunge the system to $\epsilon = -250$ µeV at point P (see Fig. 3B). Next, we rapidly pulse the system to $\epsilon = 950$ µeV (point A) with a 16 ns ramp time. After waiting for a given manipulation time, the system is pulsed back to point P in $(4,0)$. The ramp time is such that the charge transition is adiabatic, but fast enough to prepare a $(3,1)S$. Finally, we use the readout previously described to measure the triplet return probability.

Figure 3C shows the triplet return probability as a function of the manipulation time for the pulse sequence in Fig. 3A. We find a ST rotation frequency $f = 57$ MHz. This frequency is the vector sum of $J(\epsilon)$ and $A/2$, such that $hf = \sqrt{J^2 + (A/2)^2}$, where h is the Planck constant. We estimate a residual exchange of $J/h = 27$ MHz for this detuning from numeric fits to the frequency dependence on detuning described below. The inset shows that this frequency is very stable over time. Such behavior differs from GaAs systems, for which dynamic nuclear polarization must be used to generate and maintain a particular
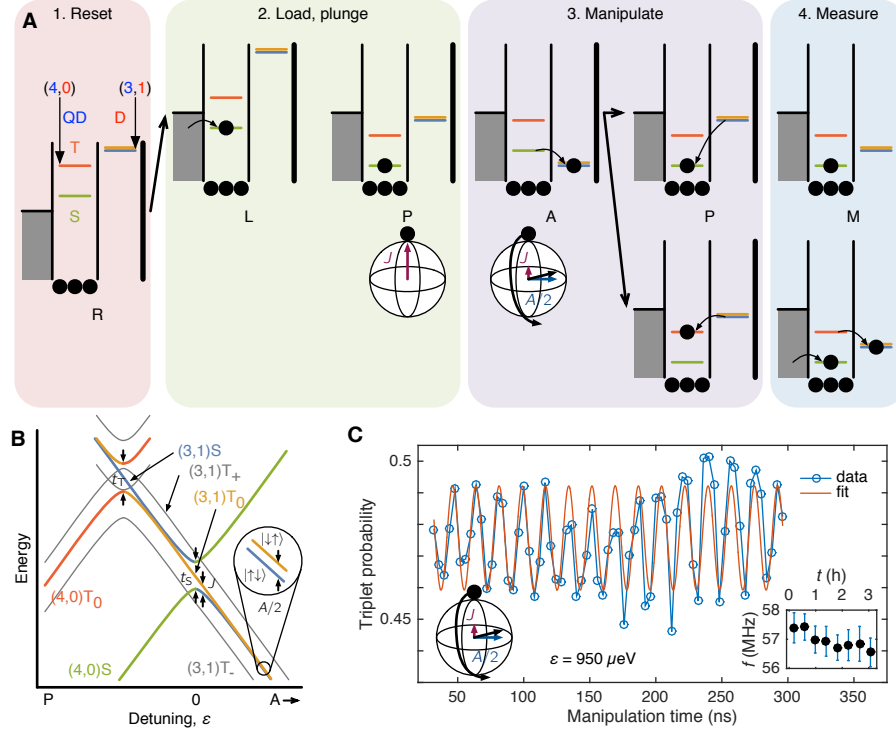
Figure 3. Hyperfine ST rotations. (**A**) Pulse sequence for the spin manipulations. The system is initialized as $(4,0)S$ and plunged to point P. Then, the detuning is pulsed rapidly to point A, which yields a separated $(3,1)S$. After a given manipulation time in $(3,1)$, which rotates the spin between S and T_0, it is pulsed back to point P. The state is then either $(4,0)S$ or $(4,0)T_0$, and is measured by going to point M. (**B**) System states and energies versus detuning, showing points P and A, and modeled as an effective $(2,0) - (1,1)$ ST qubit. (**C**) Triplet probability versus manipulation time. The oscillation frequency is $f = 56.9$ MHz. This is not the bare hyperfine frequency due to a residual exchange of $J/h = 27$ MHz, see Fig. 4C. Inset: Frequency of the oscillations for repeated measurements over 3 hours. Each point represents data averaged over 22 minutes.

ΔB_z of similar magnitude [32]. The magnitude and stability of f provides a strong indication that the rotations are driven by a single ^{31}P. A small and relatively constant frequency drift of around 0.8 MHz is observed over a period of 3.5 h. We have measured a constant drift in the electrostatics of the device such that the detuning drifts around $+4.5$ μeV/h for a fixed voltage manipulation point. This is expected to produce a frequency shift of -0.17 MHz/h through the experimentally measured $dJ/d\epsilon$ relation (see Fig. 4C), yielding a 0.6 MHz drift for the experiment's duration. Hence this f drift is consistent with a slow $J(\epsilon)$ drift. Additionally, the 0.8 MHz "dispersion" is less than natural silicon, which has linewidths greater than 8 MHz for single donors [33] and is qualitatively consistent with an enriched ^{28}Si background. Electron spin resonance (ESR) linewidths of single donors with similar enrichment levels are reported to be of order of 5 kHz [4], which provides a limit on the dispersion that might be measured if J was noise-free. Noise in J is believed to presently limit the linewidth, discussed below in terms of T_2^*.

The detuning dependence of the ST rotations reveals additional information about this QD-D system. In Fig. 4A, we plot the triplet return probability against both detuning and manipulation time. As the detuning gets closer to zero, the frequency of the exchange rotations increases, as shown in Fig. 4C. This is consistent with a ST model where the exchange energy J between the S and T_0 states is not negligible and drives rotations around a tilted axis in the qubit Bloch sphere. To better understand the exact shape of the oscillations of Fig. 4A, we simulate the quantum dynamics of the system using a master equation approach and time-dependent controls. We describe the system using the basis states $\{(4,0)S, (4,0)T_0, (3,1)S, (3,1)T_0\}$, similarly to previous treatments such as Taylor *et al.* [16]. The details of the model are given in the Supplementary Material. The numerical simulation results are shown in Fig. 4B. The phase and shape of the oscillations is very well reproduced; however, the mechanism limiting the visibility is not well understood and will be addressed in future work. The key fitting parameters of this model are the triplet tunnel coupling t_T, singlet tunnel coupling t_S, and hyperfine interaction A. We can determine these parameters using a fit to the data of Fig. 4C, knowing that hf equals the energy gap between the S and T_0 states. We find $t_S = 19$ μeV, $t_T = 31$ μeV and $A/2h = 50$ MHz. Shifts in
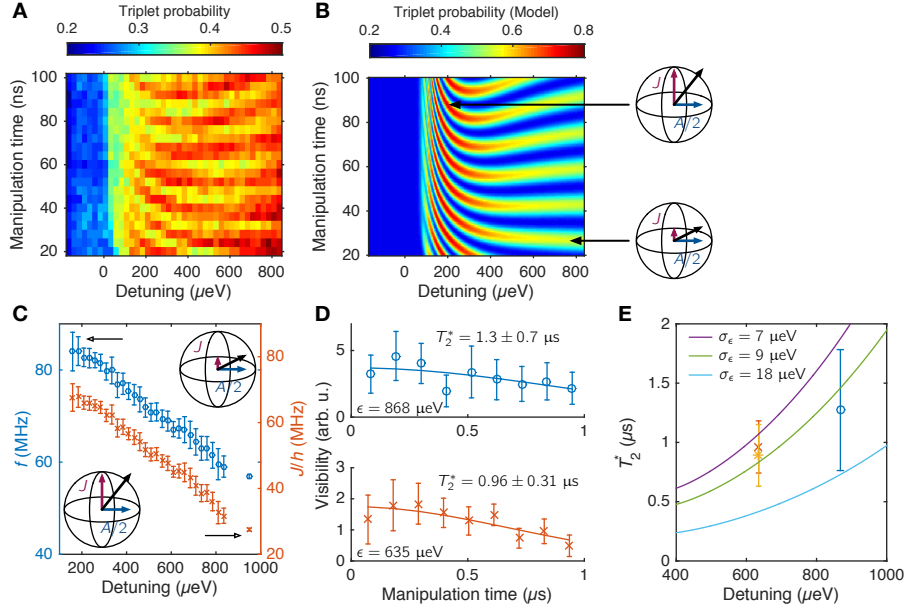
Figure 4. Detuning dependence of exchange. (**A-B**) Experimental (A) and model (B) triplet probability versus detuning and manipulation time. The oscillations on the time axis are the hyperfine-driven rotations. The phase and shape of the oscillations are well reproduced; however, the mechanism limiting the visibility is not well understood and will be addressed in future work. (**C**) Left axis: Frequency f of the oscillations versus detuning, extracted from fits to Fig. 4A. This corresponds to the $S - T_0$ energy gap, allowing a fit for model parameters $t_S = 19$ μeV, $t_T = 31$ μeV and $A/2h = 50$ MHz. Right axis: Exchange J calculated from the frequency after removing the hyperfine contribution $J/h = \sqrt{f^2 - (A/2)^2}$. (**D**) Visibility of ST rotations versus time, and T_2^* fit with a Gaussian decay model. (**E**) The T_2^* at both detunings is consistent with residual exchange and a detuning noise of $\epsilon = 9$ μeV.

A of this magnitude relative to the bulk value (58.5 MHz, [33]) have been reported in single donor ESR experiments [4] and have been attributed to Stark shifts of the contact hyperfine interaction due to the large electric fields in the vicinity of the neighboring QD. The measured value in this work is both consistent with a shallow phosphorus donor and is inconsistent with likely alternatives, such as stray arsenic. Following the fit procedure, we can extract $J(\epsilon)$ by subtracting the $A/2$ contribution. The result is shown in Fig. 4C.

Decoherence of MOS QDs [34] and single donors [4] has been characterized in separate systems, but the charge noise and magnetic noise properties of strongly hybridized QD-D systems are not well established. Our system provides a unique platform to study these important properties in an effective two-electron case where entanglement is delocalized in the form of a spatially separated singlet or triplet. We measure long time traces and plot the visibility of the oscillations versus manipulation time t in Fig. 4D. The data and method are presented in the Supplementary Material. We then fit the decay using a slow detuning noise model that produces a Gaussian decay of the visibility $v = v_0 \exp\left[-(t/T_2^*)^2\right]$, where v_0 is an arbitrary initial visibility. We find that T_2^* depends on the detuning (Fig. 4E). To understand this dependence, we use a charge noise model represented by ϵ noise with a characteristic standard deviation σ_ϵ and producing

decoherence through $J(\epsilon)$ [35]. Details are given in the Supplementary Material. We find that $\sigma_\epsilon = 9$ μeV is consistent with the observed T_2^* and that $2\sigma_\epsilon$ matches approximately the electronic temperature. In this model, we neglect magnetic noise that could be caused by residual ^{29}Si or other sources. Our observations are consistent with T_2^* being limited by charge noise, a mechanism that is expected to play an important role when J varies as a function of ϵ [35].

In summary, we have demonstrated coherent ST rotations in a coupled QD-D system in enriched ^{28}Si. The rotations are driven by the contact hyperfine interaction and produce 10 ns $X(\pi)$ rotations with a T_2^* of 1.3±0.7 μs. A charge noise model suggests that this could possibly be improved to beyond 10 μs by operating at larger detunings where the exchange is negligible. Our experiments demonstrate the feasibility of using the QD-D system as a compact ST qubit with a single QD and a built-in magnetic field gradient, and suggest that high fidelity X rotations are possible. More sophisticated ST qubit control approaches [36, 37] may likely increase the performance of a future two-axis QD-D qubit demonstration. Beyond individual ST qubits, this work opens-up compelling possibilities. One such example is the coupling of donor-based qubits without atomic precision placement through, for example, electrostatic coupling between ST qubits [38, 39]. Another example is all-electrical nuclear

spin readout [9] and electric/nuclear magnetic resonance control without high magnetic fields or ESR.

ACKNOWLEDGEMENTS

SUPPLEMENTARY MATERIALS

1. Device Fabrication and Measurement.
2. Few electron regime.
3. Pulse sequence, loading and relaxation rates.
4. Probability calibration.
5. Singlet-triplet dynamics model.
6. Detuning noise model.
7. Visibility analysis.
8. Author Contributions.
9. Figures S1-S3.
10. Tables S1.

---

* Corresponding author: P.Collard@USherbrooke.ca

† Corresponding author: mscarro@sandia.gov

[1] F. A. Zwanenburg, A. S. Dzurak, A. Morello, M. Y. Simmons, L. C. L. Hollenberg, G. Klimeck, S. Rogge, S. N. Coppersmith, and M. A. Eriksson, Rev. Mod. Phys. **85**, 961 (2013).

[2] W. M. Witzel, M. S. Carroll, A. Morello, L. Cywiński, and S. Das Sarma, Phys. Rev. Lett. **105**, 187602 (2010).

[3] A. M. Tyryshkin, S. Tojo, J. J. L. Morton, H. Riemann, N. V. Abrosimov, P. Becker, H.-J. Pohl, T. Schenkel, M. L. W. Thewalt, K. M. Itoh, and S. A. Lyon, Nat Mater **11**, 143 (2012).

[4] J. T. Muhonen, J. P. Dehollain, A. Laucht, F. E. Hudson, R. Kalra, T. Sekiguchi, K. M. Itoh, D. N. Jamieson, J. C. McCallum, A. S. Dzurak, and A. Morello, Nat Nano **9**, 986 (2014).

[5] B. E. Kane, Nature **393**, 133 (1998).

[6] E. Bielejec, J. A. Seamons, and M. S. Carroll, Nanotechnology **21**, 085201 (2010).

[7] B. Weber, Y. H. M. Tan, S. Mahapatra, T. F. Watson, H. Ryu, R. Rahman, L. C. L. Hollenberg, G. Klimeck, and M. Y. Simmons, Nat Nano **9**, 430 (2014).

[8] J. P. Dehollain, J. T. Muhonen, K. Y. Tan, A. Saraiva, D. N. Jamieson, A. S. Dzurak, and A. Morello, Phys. Rev. Lett. **112**, 236801 (2014).

[9] B. E. Kane, N. S. McAlpine, A. S. Dzurak, R. G. Clark, G. J. Milburn, H. B. Sun, and H. Wiseman, Phys. Rev. B **61**, 2961 (2000).

[10] A. J. Skinner, M. E. Davenport, and B. E. Kane, Phys. Rev. Lett. **90**, 087901 (2003).

[11] V. Srinivasa, H. Xu, and J. M. Taylor, Phys. Rev. Lett. **114**, 226803 (2015).

[12] G. Pica, B. W. Lovett, R. N. Bhatt, T. Schenkel, and S. A. Lyon, ArXiv e-prints (2015), arXiv:1506.04913 [cond-mat.mes-hall].

[13] G. Tosi, F. A. Mohiyaddin, S. B. Tenberg, R. Rahman, G. Klimeck, and A. Morello, ArXiv e-prints (2015), arXiv:1509.08538 [cond-mat.mes-hall].

[14] J. Levy, Phys. Rev. Lett. **89**, 147902 (2002).

[15] J. R. Petta, A. C. Johnson, J. M. Taylor, E. A. Laird, A. Yacoby, M. D. Lukin, C. M. Marcus, M. P. Hanson, and A. C. Gossard, Science **309**, 2180 (2005).

[16] J. M. Taylor, J. R. Petta, A. C. Johnson, A. Yacoby, C. M. Marcus, and M. D. Lukin, Phys. Rev. B **76**, 035315 (2007).

[17] M. Pioro-Ladrière, T. Obata, Y. Tokura, Y. S. Shin, T. Kubo, K. Yoshida, T. Taniyama, and S. Tarucha, Nat Phys **4**, 776 (2008).

[18] X. Wu, D. R. Ward, J. R. Prance, D. Kim, J. K. Gamble, R. T. Mohr, Z. Shi, D. E. Savage, M. G. Lagally, M. Friesen, S. N. Coppersmith, and M. A. Eriksson, Proceedings of the National Academy of Sciences **111**, 11938 (2014).

[19] L. Gaudreau, G. Granger, A. Kam, G. C. Aers, S. A. Studenikin, P. Zawadzki, M. Pioro-Ladriere, Z. R. Wasilewski, and A. S. Sachrajda, Nat Phys **8**, 54 (2012).

[20] B. M. Maune, M. G. Borselli, B. Huang, T. D. Ladd, P. W. Deelman, K. S. Holabird, A. A. Kiselev, I. Alvarado-Rodriguez, R. S. Ross, A. E. Schmitz, M. Sokolich, C. A. Watson, M. F. Gyure, and A. T. Hunter, Nature **481**, 344 (2012).

[21] L. A. Tracy, T. M. Lu, N. C. Bishop, G. A. Ten Eyck, T. Pluym, J. R. Wendt, M. P. Lilly, and M. S. Carroll, Applied Physics Letters **103**, 143115 (2013).

[22] E. Nielsen, E. Barnes, J. P. Kestner, and S. Das Sarma, Phys. Rev. B **88**, 195131 (2013).

[23] A. P. Higginbotham, F. Kuemmeth, M. P. Hanson, A. C. Gossard, and C. M. Marcus, Phys. Rev. Lett. **112**, 026801 (2014).

[24] S. Tarucha, D. G. Austing, T. Honda, R. J. van der Hage, and L. P. Kouwenhoven, Phys. Rev. Lett. **77**, 3613 (1996).

[25] R. Potok, J. Folk, C. Marcus, V. Umansky, M. Hanson, and A. Gossard, Phys. Rev. Lett. **91**, 016802 (2003).

[26] M. Xiao, M. G. House, and H. W. Jiang, Applied Physics Letters **97**, 032103 (2010).

[27] A. C. Johnson, J. R. Petta, J. M. Taylor, A. Yacoby, M. D. Lukin, C. M. Marcus, M. P. Hanson, and A. C. Gossard, Nature **435**, 925 (2005).

[28] N. S. Lai, W. H. Lim, C. H. Yang, F. A. Zwanenburg, W. A. Coish, F. Qassemi, A. Morello, and A. S. Dzurak, Sci. Rep. **1** (2011).

[29] W. H. Lim, C. H. Yang, F. A. Zwanenburg, and A. S. Dzurak, Nanotechnology **22**, 335704 (2011).

[30] C. H. Yang, A. Rossi, N. S. Lai, R. Leon, W. H. Lim, and A. S. Dzurak, Applied Physics Letters **105**, 183505 (2014).

[31] S. A. Studenikin, J. Thorgrimson, G. C. Aers, A. Kam, P. Zawadzki, Z. R. Wasilewski, A. Bogan, and A. S. Sachrajda, Applied Physics Letters **101**, 233101 (2012).

[32] C. Barthel, J. Medford, H. Bluhm, A. Yacoby, C. M. Marcus, M. P. Hanson, and A. C. Gossard, Phys. Rev. B **85**, 035306 (2012).

[33] J. J. Pla, K. Y. Tan, J. P. Dehollain, W. H. Lim, J. J. L. Morton, D. N. Jamieson, A. S. Dzurak, and A. Morello, Nature **489**, 541 (2012).

[34] M. Veldhorst, J. C. C. Hwang, C. H. Yang, A. W. Leenstra, B. de Ronde, J. P. Dehollain, J. T. Muhonen, F. E. Hudson, K. M. Itoh, A. Morello, and A. S. Dzurak, Nat Nano **9**, 981 (2014).

[35] O. E. Dial, M. D. Shulman, S. P. Harvey, H. Bluhm, V. Umansky, and A. Yacoby, Phys. Rev. Lett. **110**, 146804 (2013).

[36] M. D. Shulman, S. P. Harvey, J. M. Nichol, S. D. Bartlett, A. C. Doherty, V. Umansky, and A. Yacoby, Nat Commun **5** (2014).

[37] P. Cerfontaine, T. Botzem, D. P. DiVincenzo, and H. Bluhm, Phys. Rev. Lett. **113**, 150501 (2014).

[38] J. E. Levy, M. S. Carroll, A. Ganti, C. A. Phillips, A. J. Landahl, T. M. Gurrieri, R. D. Carr, H. L. Stalford, and E. Nielsen, New Journal of Physics **13**, 083021 (2011).

[39] M. D. Shulman, O. E. Dial, S. P. Harvey, H. Bluhm, V. Umansky, and A. Yacoby, Science **336**, 202 (2012).

[40] B. Bertrand, H. Flentje, S. Takada, M. Yamamoto, S. Tarucha, A. Ludwig, A. D. Wieck, C. Bäuerle, and T. Meunier, Phys. Rev. Lett. **115**, 096801 (2015).

Supplementary Material for: Nuclear-driven electron spin rotations in a single donor coupled to a silicon quantum dot

DEVICE FABRICATION AND MEASUREMENT

The device used for these experiments is fabricated identically to the one of Fig. 1A. Electrons are confined in a 2D electron gas at the interface between an epitaxial enriched ^{28}Si layer with 500 ppm residual ^{29}Si and a 35 nm gate oxide. Highly n-doped poly-silicon gates (200 nm thick) are patterned on top of the gate oxide using low pressure chemical vapor deposition and plasma etching [21]. These are used to accumulate electrons by applying a positive voltage (in an enhancement mode) or deplete electrons (with negative voltages). Phosphorus donors are implanted in a PMMA resist window that overlaps with the AG gate on both sides of both wires, and the poly-Si gate used as a self-aligned implantation mask. The approximate relevant donor location indicated by the red dot in Fig. 1A of the main text is inferred from various donor-gate capacitance ratios. The source and drain reservoir electrons are connected by n+ regions and ohmic contacts to the instruments. The device is biased to form a SET in the upper wire that is used as a charge sensor (CS), while simultaneously forming a few-electron QD under the lower wire. The CS current I_{CS} is measured using an AC lock-in technique at 403 Hz with 0 DC source-drain bias and 100 µV (rms) AC bias. The derivative with respect to gate voltage is taken numerically to show the QD charge occupancy steps in charge stability diagrams.

FEW ELECTRON REGIME

One can form a clean single QD with this device geometry through biasing that pushes the QD towards one lead, shown in Fig. S1A. A representative set of gate voltages used for this experiment is shown in Fig. S1C. We use gates AG and CP to discriminate between QD and D states, respectively. The region where donors interact resonantly with the QD is shown in Fig. S1B. In this regime, the single QD turns into two strongly coupled QDs in series along the wire axis. This is indicated in the charge stability diagram of Fig. S1B by two sets of nearly parallel lines. This behavior is systematically reproduced in the devices we measured with such a geometry, which indicates that it is a feature produced by the electrostatics of the device. We can assign occupation numbers to the two QDs, counting from zero. We establish that the QD is in the few electron regime (i.e. emptied) by opening the tunnel barriers to the point where the QD charge-sensed lines become lifetime-broadened without detecting other states (data not shown). We additionally performed magnetospectroscopy [24–26] to verify that the first electron

fills as a spin-down electron. For this work, we treat the QD closest to the reservoir as being part of the reservoir itself and neglect its impact on the other QD.

PULSE SEQUENCE, LOADING AND RELAXATION RATES

The AC component of pulses in the experiment is applied using an Agilent 33500B arbitrary waveform generator using two synchronized channels for the AG and CP gates. The waveform is composed of DC and AC components and applied to the gates through a room temperature bias tee. The waveforms are applied such that all target points are fixed in the charge stability diagram, except the ones explicitly varied for a particular measurement (e.g. manipulation time or position of point M). The $(4,0)S$ loading rate is approximately $1/(60$ µs$)$, and the $(4,0)T$ loading rate approximately $1/(6$ µs$)$. The $(4,0)T \rightarrow (4,0)S$ relaxation time is approximately 375 µs, determined by preparing mostly $(4,0)T$ and measuring the triplet probability decay versus time. The metastable state lifetime is roughly 2 to 4 ms.

Table S1. Pulse sequence parameters. Table of pulse sequence points (as defined in main text Fig. 1C), ramp time to point (from previous point), and wait time at point, for a typical manipulation pulse sequence used. The sequence is played in a loop.

Point	Ramp time (µs)	Wait time (µs)
R	10	50
L	0.1	150
P	1	0.2
A	0.016	0.1
P	0.016	0.2
M	10	350

PROBABILITY CALIBRATION

To calibrate the triplet probability, the following procedure is used. First, the CP gate voltage of the measurement point M and the loading point L are swept to tune the readout and initialization, respectively, using the same waveform as for state manipulation except for point A (such that no manipulations are done). The resulting CS current is mapped in Fig. S2A. Given a certain load level, the CS current is then plotted versus CP measurement level, Fig. S2B. The current has a downward linear trend because of the CS Coulomb peak flank and a step that is similar in origin to a normal charge sensing signal. To the left of the measurement window the current always
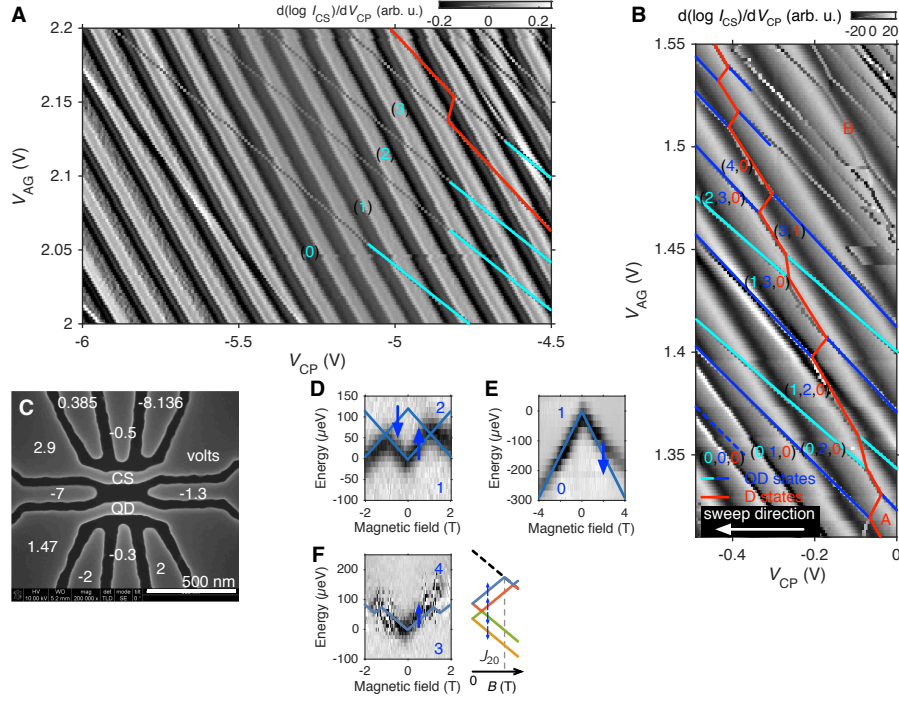
Figure S1. Quantum dot and donor states. (**A**) Single dot regime. (**B**) Charge stability diagram showing all states. Notation: $(QD2, QD, D)$. The QD2 represents a QD that is strongly coupled to the lead and is ignored in the main text. (**C**) Typical gate voltages for the experiment. (**D-E**) Opening the QD-lead tunnel barriers allows to probe the spin filling of the first two QD states through magnetospectroscopy. CP gate voltage has been converted to energy using a lever arm. (**F**) Magnetospectroscopy data showing the $(3,0) \leftrightarrow (4,0)$ transition loading as a spin singlet. The $(4,0)$ ground state hence forms an effective $(2,0)S$ with exchange splitting $J_{40} = 143$ μeV (confirmed with pulse spectroscopy). The CP gate voltage was converted to energy E through the lever arm. Grey scale: dI_{CS}/dE (arb. u.). Right schematic: The observed spin filling is qualitatively consistent with a simple shell filling model.

corresponds to a singlet signal, and to the right it always corresponds to a triplet signal. By extrapolating what this current would be assuming a linear background, one can determine what the pure singlet and triplet signals should be in the measurement window. The actual triplet probability is determined using a linear transformation that maps I_{CS} to triplet probability. When manipulations are performed, the duty cycle of the waveform is changed by at most 0.2%, so the calibration is largely unaffected. Any systematic error introduced by this method (e.g. broadening of transitions due to temperature) would tend to underestimate the visibility of oscillations.

SINGLET-TRIPLET DYNAMICS MODEL

We model the ST system with a 4×4 Hamiltonian in the basis $\{|(4,0)S\rangle, |(4,0)T_0\rangle, |(3,1)S\rangle, |(3,1)T_0\rangle\}$ given by

$$H(t) = \frac{1}{2} \begin{pmatrix} \epsilon(t) & 0 & -t_S & 0 \\ 0 & 2J_{40} + \epsilon(t) & 0 & -t_T \\ -t_S & 0 & -\epsilon(t) & -A/2 \\ 0 & -t_T & -A/2 & 2J_{31} - \epsilon(t) \end{pmatrix}, \quad (1)$$
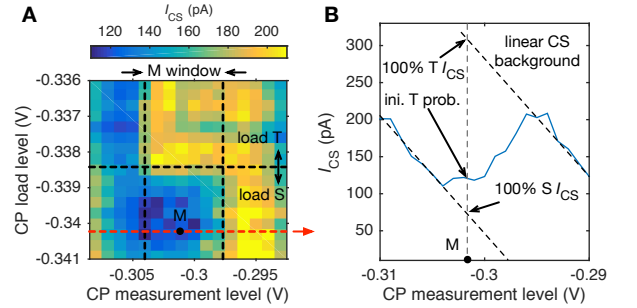

Figure S2. Probability calibration. (**A**) The CP gate voltage of measurement point M and loading point L are swept to tune the readout and initialization, respectively, using the same waveform as for state manipulation except for point A (no manipulations). This method allows to map the measurement and initialization windows. (**B**) A cut through measurement levels reveals what the current would be fore pure S or T states in the measurement window.

where J_{40} and J_{31} are the exchange between singlet and triplet states in the $(4,0)$ and $(3,1)$ charge sectors, respectively, t_S (t_T) is the QD-D tunnel coupling for the singlet (triplet) states, $A/2$ is the effective magnetic field gradient due to the contact hyperfine interaction in the $(3,1)$ con-

figuration, and $\epsilon(t)$ is the detuning. We fix $J_{40} = 143$ μeV and $J_{31} = 0$ μeV. For a given control schedule $\epsilon(t)$, we numerically integrate to solve for the time evolution of the density matrix $\rho(t)$ generated by the von Neumann equation

$$\frac{\mathrm{d}\rho(t)}{\mathrm{d}t} = -\frac{i}{\hbar}\left[H(t), \rho\right]. \tag{2}$$

To model the effect of finite control bandwidth, the pulse sequence we consider in our numerical simulations is given by the ideal pulse sequence after having been filtered through a (low pass) RC filter,

$$\tilde{\epsilon}(t) = \int_{-\infty}^{\infty} \mathrm{d}\tau\, h_{\mathrm{RC}}(\tau)\epsilon(t - \tau), \tag{3}$$

where $h_{\mathrm{RC}}(\tau) = \frac{1}{RC}\theta(t)\,\mathrm{e}^{-t/RC}$ is the impulse response function and $\theta(t)$ is the Heaviside step function. Considering various filtered control schedules $\tilde{\epsilon}(t)$, we find that a time constant $1/RC = 10$ ns is consistent with the experiment.

DETUNING NOISE MODEL

Since our device is fabricated with enriched ^{28}Si, the fluctuations in the "magnetic" control axis $A/2$ are expected to be small. Other work in ST qubits has shown that a dominant mechanism limiting the coherence is noise in exchange $J(\epsilon)$ induced by quasi-static noise on the detuning $\epsilon \rightarrow \epsilon + \eta$ [35, 40], i.e. "charge" noise. Given a quasi-static noise on the detuning η having zero mean and standard deviation σ_ϵ, an ensemble average leads to a Gaussian decay of the coherence of the form

$$C(t) = \int_{-\infty}^{\infty} \mathrm{d}\eta P(\eta) \cos\left(\frac{t\Delta(\epsilon + \eta)}{\hbar}\right) \tag{4}$$

$$= \exp\left[-\left(\frac{t}{T_2^*}\right)^2\right]\cos\left(\frac{t\Delta(\epsilon)}{\hbar}\right), \tag{5}$$

where $P(\eta) = \mathrm{e}^{-\eta^2/2\sigma_\epsilon^2}/\sqrt{2\pi}\sigma_\epsilon$, $\Delta(\epsilon)$ is the energy gap $\Delta(\epsilon) = \sqrt{J^2 + (A/2)^2}$, and

$$T_2^* = \frac{\sqrt{2}\hbar}{\sigma_\epsilon\left|\partial\Delta/\partial\epsilon\right|}. \tag{6}$$

Since the values we report for T_2^* pertain to an ensemble average of measurements over a timescale of hours, our estimated detuning noise strength includes the effects of a secular drift component as well. While sufficiently large variations of the detuning can lead to Stark shifting of

the contact hyperfine strength A, this Stark shifting effect should be small compared to the $\sigma_\epsilon \sim 10$ μeV that we observe.

VISIBILITY ANALYSIS

To extract the visibility v of the ST oscillations of Fig. 4D, the following method is employed. The source data is shown in Fig. S3. Because of CS drift over the long periods of time required to acquire these longer time traces, the CS current (proportional to triplet probability) has a general downward trend and some residual fluctuations. To remove these fluctuations and smooth the data, the time trace is divided into time bins of approximately 100 ns. The oscillations in each time bin are fitted with a sine function of fixed frequency. The amplitude for each time bin is then reported as visibility in Fig. 4D. The visibility decay is then fitted using a Gaussian decay, as detailed in the "Detuning noise model" section. We have verified that this time binning method agrees well with other methods such as maximum likelihood analysis. We now look at the apparent modulations of the oscillations in Fig. 3C of the main text and Fig. S3. These are believed to arise from the averaging of a limited ensemble of traces with slightly different frequencies. This is expected because of the slow charge noise and light drift, and leads to beating-like features. We also calculate the Fourier transform of the data to verify the spectral content of the signal and find a single large peak at the expected frequency.
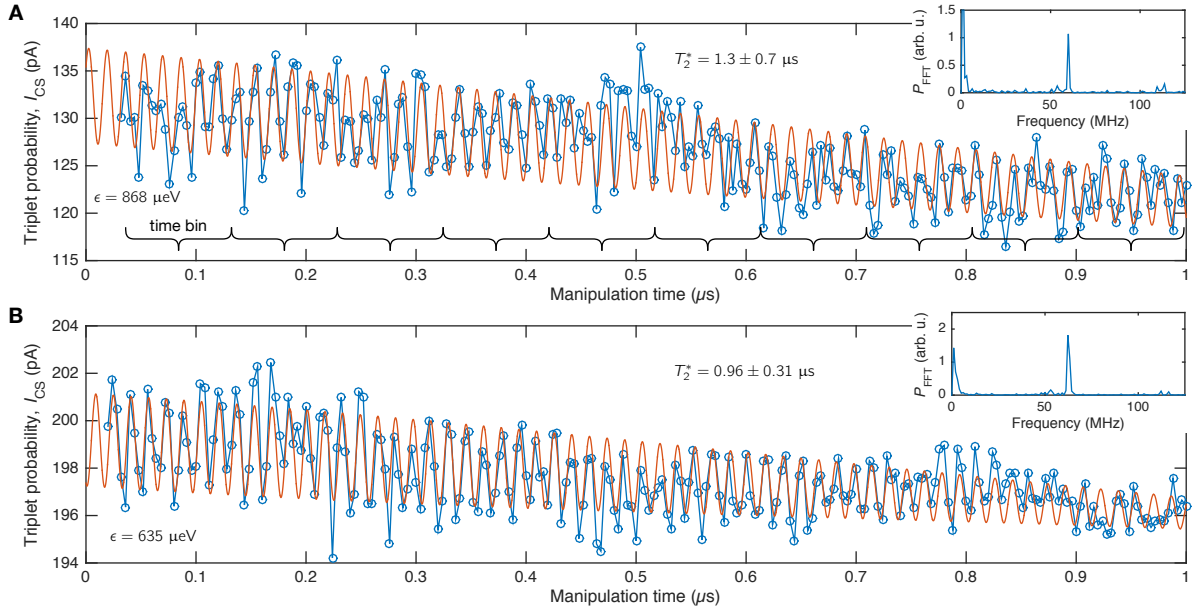
AUTHOR CONTRIBUTIONS

Figure S3. Long ST rotations. (**A-B**) ST oscillations used to extract the visibility and T_2^*. The visibility as a function of time is determined by the amplitude of a sine fit for each time bin separately (not shown). The overlay fit curve is a sinusoidal fit with Gaussian decay that has good agreement with the data and the time binning method. Insets: Fast Fourier Transform power (P_{FFT}) spectrum showing a clear single-frequency signal.